2nd Advanced Optical Metrology Compendium

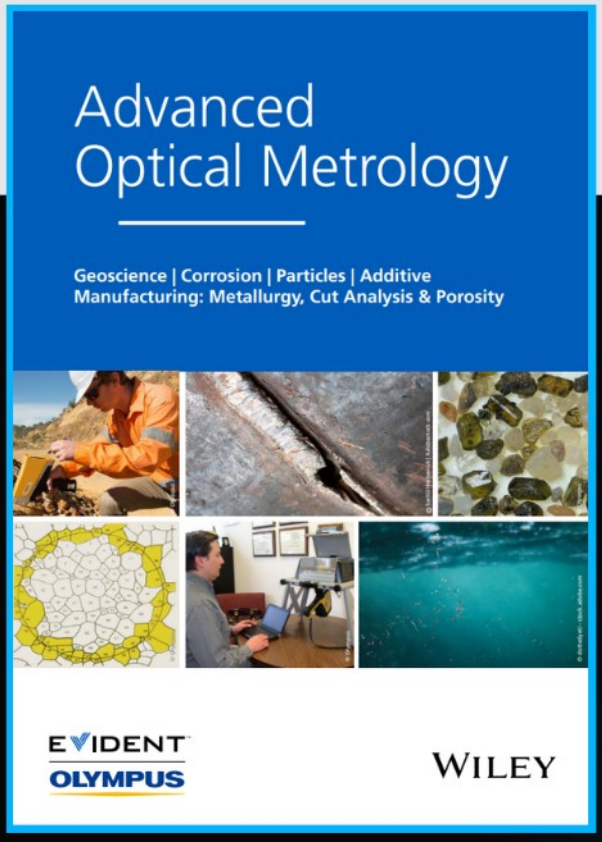

The latest eBook from Advanced Optical Metrology. Download for free.

This compendium includes a collection of optical metrology papers, a repository of teaching materials, and instructions on how to publish scientific achievements.

With the aim of improving communication between fundamental research and industrial applications in the field of optical metrology we have collected and organized existing information and made it more accessible and useful for researchers and practitioners.

EVIDENT
OLYMPUS

WILEY

NANO · MICRO small
www.small-journal.com

Confined Tri-Functional FeO_x@MnO_2@SiO_2 Flask Micromotors for Long-Lasting Motion and Catalytic Reactions

Yangyang Yang, Lei Shi, Jingkai Lin, Panpan Zhang, Kunsheng Hu, Shuang Meng, Peng Zhou, Xiaoguang Duan, Hongqi Sun, and Shaobin Wang**

H_2O_2-fueled micromotors are state-of-the-art mobile microreactors in environmental remediation. In this work, a magnetic FeO_x@MnO_2@SiO_2 micromotor with multi-functions is designed and demonstrated its catalytic performance in H_2O_2/peroxymonosulfate (PMS) activation for simultaneously sustained motion and organic degradation. Moreover, this work reveals the correlations between catalytic efficiency and motion behavior/mechanism. The inner magnetic FeO_x nanoellipsoids primarily trigger radical species ($^{\bullet}OH$ and $O_2^{\bullet-}$) to attack organics via Fenton-like reactions. The coated MnO_2 layers on FeO_x surface are responsible for decomposing H_2O_2 into O_2 bubbles to provide a propelling torque in the solution and generating $SO_4^{\bullet-}$ and $^{\bullet}OH$ for organic degradation. The outer SiO_2 microcapsules with a hollow head and tail result in an asymmetrical Janus structure for the motion, driven by O_2 bubbles ejecting from the inner cavity via the opening tail. Intriguingly, PMS adjusts the local environment to control overviolent O_2 formation from H_2O_2 decomposition by occupying the Mn sites via inter-sphere interactions and enhances organic removal due to the strengthened contacts and Fenton-like reactions between inner FeO_x and peroxides within the microreactor. The findings will advance the design of functional micromotors and the knowledge of micromotor-based remediation with controlled motion and high-efficiency oxidation using multiple peroxides.

1. Introduction

Artificial self-propelled micromotors with an asymmetrical structure can swim in a liquid solution under physical/chemical stimuli (e.g., light, ultrasound, magnetic field, temperature, H_2O_2, etc.).[1] As a green chemical, hydrogen peroxide can be decomposed by various metal-based materials (e.g., Pt, Ag, MnO_2, etc.)[2–4] and generate O_2 bubbles to drive micromotors. Owing to high catalytic activities (Equation (1)) and biocompatibility, MnO_2-based materials have shown advantages in the H_2O_2-fueled micromotors.[5]

$$H_2O_2 \xrightarrow{MnO_2} H_2O + \frac{1}{2}O_2 \uparrow \quad (1)$$

However, H_2O_2 decomposition to O_2 is competitive in producing hydroxyl radicals in Fenton reactions:[5] the higher conversion to O_2, the fewer radicals produced from H_2O_2 decomposition for organic removal. Such side a reaction significantly limits the application of MnO_2 micromotors in environmental catalysis.[6]

Recently, Fenton-active compounds (e.g., Fe_2O_3, Fe_3O_4) have been considered in Mn-based micromotors via physical adsorption or chemical nucleation growth to improve the catalytic activity.[7–9] SiO_2/MnO_2 tubular micromotors decorated with Fe_2O_3 nanoparticles were tested in H_2O_2-based Fenton-like reactions under visible light.[10] Magnetic MnO_2@pollen micromotors were also used to

Y. Yang, J. Lin, K. Hu, X. Duan, S. Wang
School of Chemical Engineering and Advanced Materials
The University of Adelaide
North Terrace, Adelaide, South Australia 5005, Australia
E-mail: xiaoguang.duan@adelaide.edu.au;
shaobin.wang@adelaide.edu.au

L. Shi
Joint International Research Laboratory of Biomass Energy and Materials
College of Materials Science and Engineering
Nanjing Forestry University
Nanjing 210037, China

The ORCID identification number(s) for the author(s) of this article can be found under https://doi.org/10.1002/smll.202207666.

DOI: 10.1002/smll.202207666

P. Zhang
School of Material Science and Engineering
Jiangsu University
Zhenjiang 212013, China

S. Meng, P. Zhou
College of Architecture and Environment
Sichuan University
Chengdu 610065, China

H. Sun
School of Science
Edith Cowan University
270 Joondalup Drive, Joondalup, Western Australia 6027, Australia

remove tetracycline.[11] Although the oxidation of organics was enhanced via the assistance of Fenton-active compounds, the trade-offs between motion behavior (the torque) and oxidation efficiency (on-demand catalysis) are less investigated while both are peroxide-consuming processes.[11–14] Thus, the self-propelled motions, in situ-induced micro-mixing environment, and intensified mass transfer of micromotors in water for oxygen and radical generation appeal to environmental catalysis. However, it is difficult to achieve the dual actions of simultaneously strong motion and high organic degradation of nanomotors unless increasing H_2O_2 input in the oxidation system.[11,15,16] More recently, perxymonosulfate (PMS) has been suggested for sulfate radical-based Fenton-like reaction and MnO_2 exhibited excellent performance in PMS activation.[11] Unfortunately, limit work has been applied by micromotors.

Meanwhile, various surfactants (e.g., Triton X, Tween 20, and sodium dodecyl sulfate) were generally applied to increase the hydrophilicity of micromotor surfaces for mobility.[7,15] In the remediation system, surfactants are toxic chemicals and could decrease the oxidation efficiency of organics as they would consume free radicals.[15] For avoiding the use of surfactants, porous SiO_2 or carbonaceous shells are applied to provide an open micro-environment to decompose H_2O_2 into O_2 in a solution.[17–23] The controllable shapes (e.g., flask-like or tadpole-like structures) with a regulated opening will also provide an inner cavity to accommodate H_2O_2-sensitive seeds to accelerate the mass transfer of hydrogen peroxide.[19,24,25]

In this work, we prepared a flask-like $FeO_x@MnO_2@SiO_2$ micromotor with self-propelling to degrade antibiotics in the PMS/H_2O_2 system. The micromotors with hollow tails of different lengths were developed to explore the relations between structure, velocity, and degradation efficiency. The motion behaviors of H_2O_2-fueled micromotors with different aging durations and solutions pH_0 as well as the pollutant (naproxen) degradation performance in the PMS/H_2O_2 system were comprehensively investigated to reveal the motion mechanisms. We found that PMS could not only provide extra free radicals to attack organics but also slow down the H_2O_2 decomposition, realizing a long-lasting motion during the remediation process. Through analyzing the generation and variation of reactive oxygen species (ROS) and detecting the change in solution pH, the mechanism of antibiotic removal was systematically unveiled. This work provides a new design of micromotors and their application in PMS-based Fenton reactions. Moreover, this work will provide an in-depth understanding of the complicated impacts of micromotor morphology and its components in regulating the torque, mass transfer of reactants, and peroxide concentration in the confined microenvironment to achieve long-lasting propelling and catalytic efficiency for antibiotic purification in water.

2. Results and Discussion

2.1. Design and Synthesis of $FeO_x@MnO_2@SiO_2$ Micromotors

Inspired by the free-mechanical motion of micromotors, we design a magnetic and multifunctional Fe-Mn-Si microcapsule. As shown in **Figure 1**a, α-Fe_2O_3, α-Fe_2O_3/Fe_3O_4 (defined as FeO_x), $FeO_x@MnO_2$, and $FeO_x@MnO_2@SiO_2$ were well prepared by different methods.[17,26,27] Specially, α-Fe_2O_3 nanoellipsoids (<500 nm, JCPDS No. 33–0664, Figure 1b) with a rough surface were obtained via the hydrolysis of iron chloride. Then, partial α-Fe_2O_3 was thermally reduced to magnetic Fe_3O_4 (JCPDS No. 26–1136) in H_2 atmosphere. FeO_x surface became smooth due to the lattice reconstruction (Figure 1c). After coating with lamellar δ-MnO_2 (Figure S2, Supporting Information), $FeO_x@MnO_2$ nanoellipsoids were used as seeds to trigger the growth of amorphous silica shells on MnO_2 surfaces (Figure 1d). In Figure 1e–e5, the elemental mapping showed that the surface of $FeO_x@MnO_2$ nanoellipsoids was well coated by a SiO_2 shell. In addition, after dissolving the metal components with hydrochloric acid, the individual SiO_2 shell linked with other shells, resulting in a large cluster to trigger the nucleation of SiO_2 microcapsules (Figure S3, Supporting Information). Moreover, as illustrated in Figure 1f–f5, the indirect contact between SiO_2 and MnO_2 (a remarkable gap) was due to their heterogeneous characteristics, which was conducive to the mass transfer of the solution and reactants. Notably, the $FeO_x@MnO_2@SiO_2$ clusters are located at the inner head of SiO_2 microcapsules (<2 μm) (Figure 1g–h4). This phenomenon may be related to the growth process of SiO_2 microcapsules.

To unveil the growth mechanism of SiO_2 microcapsules, we investigated the evolution of SiO_2 microcapsules with different synthesis factors, including H_2O, sodium citrate, $NH_3 \cdot H_2O$, tetraethylorthosilicate (TEOS), and aging time. In a typical mutual-template-assisted method, SiO_2 was derived from the hydrolysis of TEOS, and $NH_3 \cdot H_2O$ acted as the catalyst.[17,28] Sodium citrate would react with $NH_3 \cdot H_2O$ to form ammonium citrate as the template to trigger the nucleation and growth of SiO_2. The template was dissolved by water after the reaction, resulting in hollow SiO_2 microcapsules. The head sizes of microcapsules could be tailored by different solvents (e.g., ethanol, 1-propanol, and isopropanol), which may be due to the state of templates in various solvents.[17] Particularly, SiO_2 microcapsules formed in ethanol demonstrated the biggest inner cavity, which was more conducive to mass transfer with the surrounding solution. Thus, we used ethanol as the solvent to manufacture SiO_2 microreactors. Besides, we found that H_2O, $NH_3 \cdot H_2O$, and TEOS can promote SiO_2 growth.[17] As shown in **Figure 2**a, SiO_2 microcapsules change from condensed SiO_2 film to microcapsules with a rising content of H_2O from 1.7 to 4.7 mL, and their yield increases. Moreover, a higher loading of sodium citrate would consume more $NH_3 \cdot H_2O$, leading to a half-baked SiO_2 microcapsule due to the slower growth rate (Figure 2b). With the increased content of $NH_3 \cdot H_2O$, the template (ammonium citrate) experienced a variation in shapes or other physical features (e.g., solubility), affecting the connection between the head and tail. Finally, the structure of the tails was broken at a very high dose of $NH_3 \cdot H_2O$ (350 μL) in Figure 2c. More TEOS from 50 to 250 μL would accelerate the hydrolysis, resulting in a long tail (Figure 2d). Based on the above research, the optimal reaction conditions are 4.7 mL H_2O, 1 mL sodium citrate (0.06 M), 190 μL $NH_3 \cdot H_2O$, and 150 μL TEOS. We further investigated the influence of aging time in Figure S4, Supporting Information. The head of SiO_2 microcapsules formed an opening in 60 min; afterward, the hollow tail became longer with the increased aging duration.

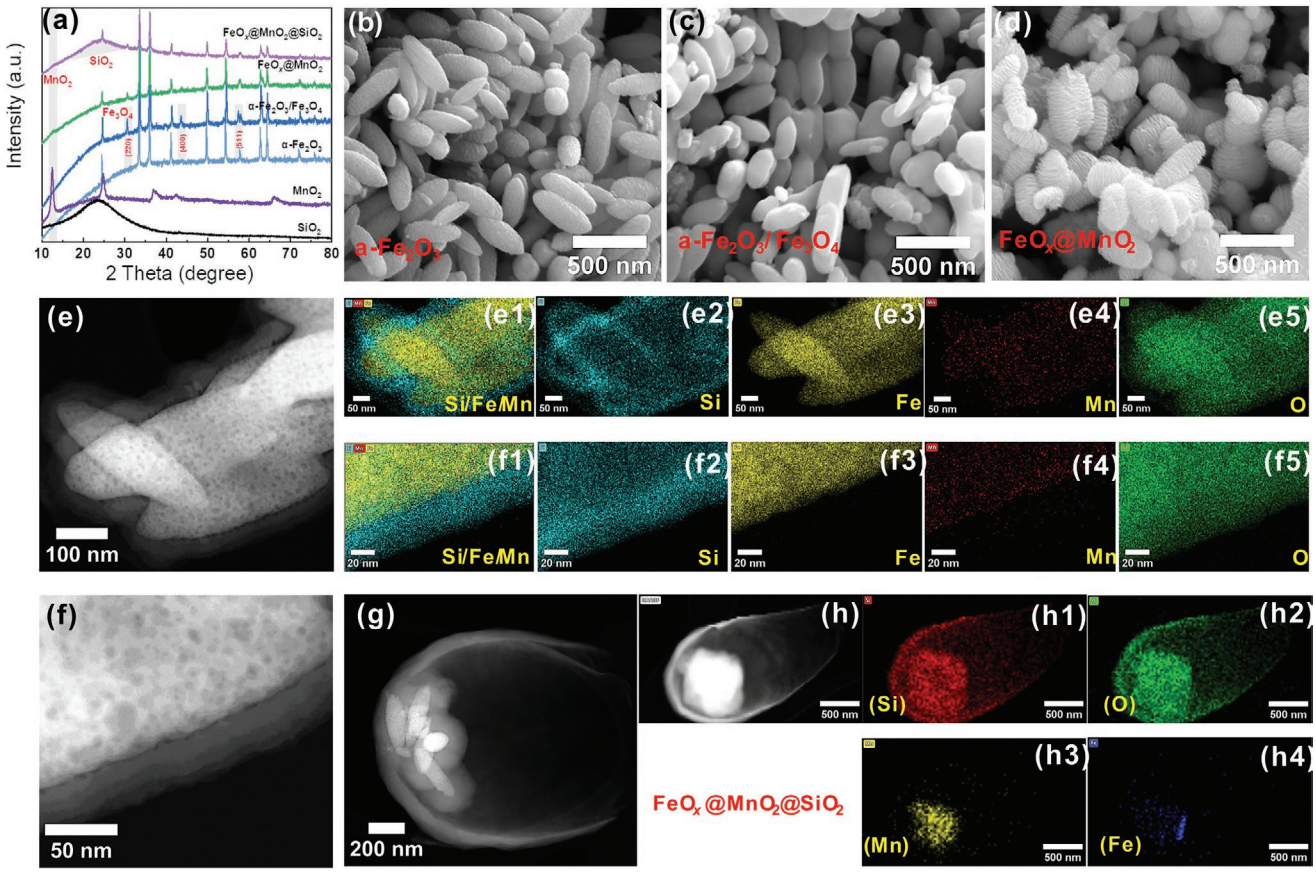

Figure 1. a) XRD patterns of α-Fe_2O_3, δ-MnO_2, SiO_2, α-Fe_2O_3/Fe_3O_4, FeO_x@MnO_2, and FeO_x@MnO_2@SiO_2; SEM images of b) α-Fe_2O_3, c) α-Fe_2O_3/Fe_3O_4, and d) FeO_x@MnO_2; e–h) STEM images with EDS mapping analysis of FeO_x@MnO_2@SiO_2.

Based on the above investigation, the SiO_2 microcapsule growth process is summarized in **Figure 3**. α-Fe_2O_3 nanoellipsoids were first prepared via the hydrolysis of iron chloride. After H_2 treatment, partial α-Fe_2O_3 was transformed into magnetic Fe_3O_4, forming FeO_x nanoellipsoids with smooth surfaces. Then the FeO_x was coated by sheet-like MnO_2 layers. Due to the lower zeta potential, FeO_x (–31.7 mV) preferably adsorbs permanganate ions compared with α-Fe_2O_3 (–28.2 mV) and grows a thicker MnO_2 lamella, as shown in Figure S5, Supporting Information. Similar results of MnO_2 growth were observed in cubic α-Fe_2O_3 (Figure S6, Supporting Information). Afterward, the porous SiO_2 shells were constructed on the MnO_2 surface via TEOS hydrolysis, which will not prevent the mass transfer and reaction between FeO_x@MnO_2 and reactants in the solution.[18] With the sustained hydrolysis of TEOS, several FeO_x@MnO_2@SiO_2 nanoellipsoids were connected by porous SiO_2, forming a larger cluster for the growth of SiO_2 microcapsules. The templates (ammonium citrate) may adsorb on the seed surfaces via the electrostatic effect and attach to the head before 45 min.[25] Then, the SiO_2 microcapsules develop a head with a cavity and a hollow tail with prolonged aging time (**Figure 4**a–f).

A similar result was also found for α-Fe_2O_3@MnO_2@SiO_2 micromotors (Figure S7, Supporting Information). Intriguingly, the MnO_2 coating was more conducive to forming SiO_2-framed seeds. As shown in Figure S8, Supporting Information, more Fe_2O_3 individuals did not construct α-Fe_2O_3@SiO_2 micromotors but exposing the active compounds outsides, which may be due to the good dispersion and small sizes of α-Fe_2O_3 nanoellipsoids (Figure S9, Supporting Information). However, seed over-aggregation would affect the purity of FeO_x@MnO_2@SiO_2 micromotors. As shown in Figure S10, Supporting Information, further increasing the loading of FeO_x@MnO_2 nanoellipsoids led to severe aggregation and massive empty SiO_2 microcapsules. To achieve the optimal utilization of SiO_2 microcapsules, we added 0.13 mL of FeO_x@MnO_2 slurry (10 mg mL^{-1}) during the synthesis of FeO_x@MnO_2@SiO_2 micromotors.

2.2. Evaluation of Motion Behavior of FeO_x@MnO_2@SiO_2 Micromotors

The mobility of FeO_x@MnO_2@SiO_2 micromotors was examined by an optical microscope. MnO_2 is an effective catalyst for H_2O_2 decomposition (the fuel) to produce O_2 bubbles (the torque) via Equation (1). Upon reacting with H_2O_2, massive O_2 bubbles are released into the solution from the surface of FeO_x@MnO_2@SiO_2 clusters in the microreactor. The SiO_2 microcapsules with an asymmetric structure direct the airflow through the opening at the tail. Then, generated O_2 bubbles propel the micromotors to move automatically in the solution. Due to the porous structures of amorphous SiO_2, no surfactant

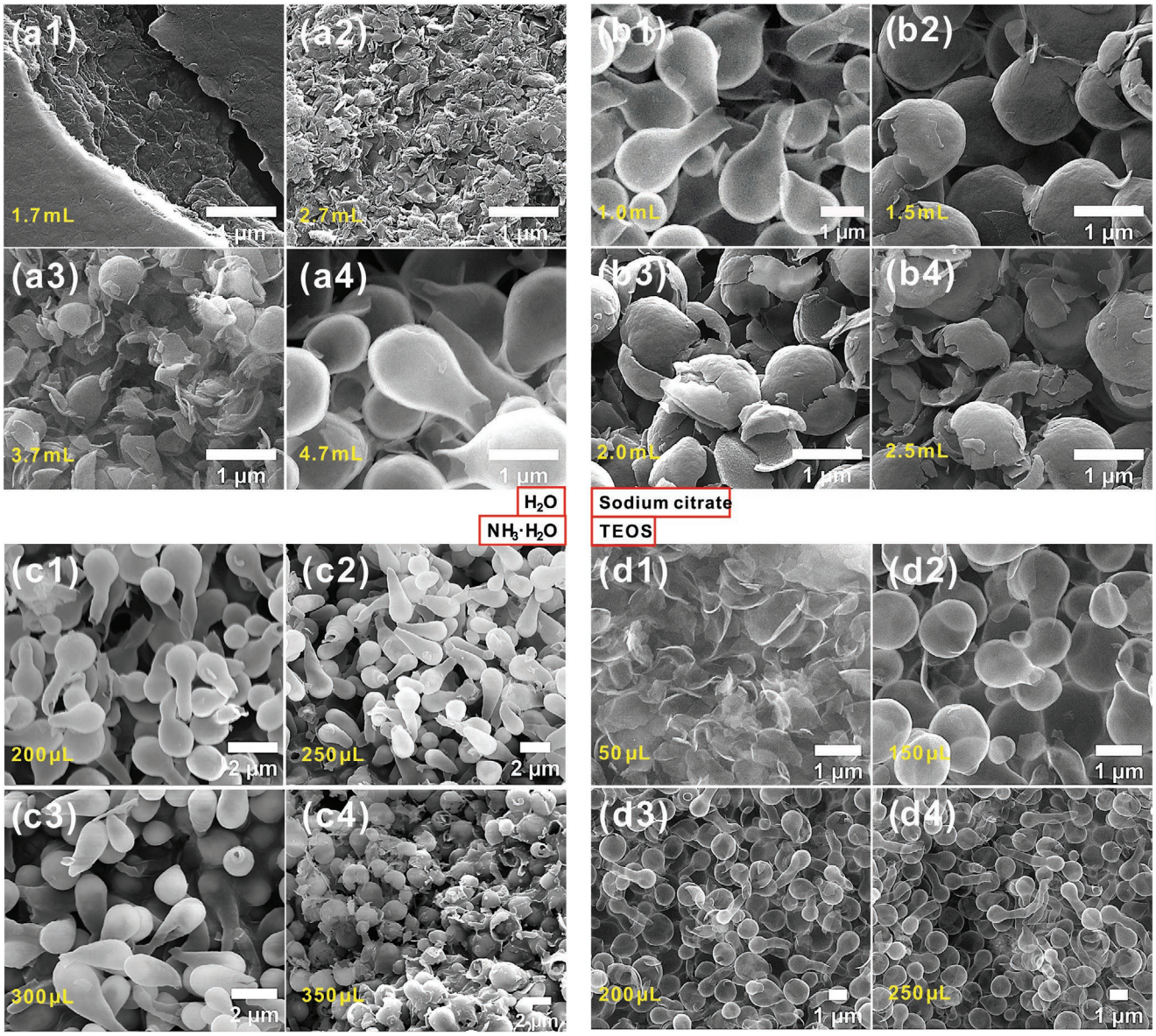

Figure 2. SEM images of SiO_2 microcapsules with different growth factors: a) H_2O, b) sodium citrate, c) $NH_3{\cdot}H_2O$, and d) TEOS.

(e.g., sodium dodecyl sulfate) was applied to enhance motion behaviors. Because the large opening is favorable for mass transfer, two micromotors prepared at an aging duration of 75 min (FeO_x@MnO_2@SiO_2-75 min (Figure 4c) and Fe_2O_3@MnO_2@SiO_2-75 min (Figure S7c, Supporting Information)) were selected to analyze the self-driven movement in 1 wt% H_2O_2 aqueous solution.

Figure 5a presents diverse locomotion trajectories of FeO_x@MnO_2@SiO_2 micromotors in the H_2O_2 solution, including linear, orbital, rotary, and helical modes (Video S1, Supporting Information). The non-directionality could be tailored by the magnetic Fe_3O_4 components in FeO_x. As shown in Figure 5b, O_2-propelled micromotors can swim following the magnetic guidance in the solution (Video S2, Supporting Information). However, partial empty flask-like SiO_2 shells did not respond to the magnet due to the absence of the active core (FeO_x@MnO_2). The mean velocity of FeO_x@MnO_2@SiO_2-75 min and Fe_2O_3@MnO_2@SiO_2-75 min samples were also evaluated at different H_2O_2 concentrations (1–15 wt%) without controlling solution pH_0. Figure 5c shows that Fe_2O_3@MnO_2@SiO_2 micromotors experienced an insignificant variation at increased H_2O_2 concentrations. In contrast, FeO_x@MnO_2@SiO_2 micromotors ran faster upon introducing more H_2O_2. The mean velocity of FeO_x@MnO_2@SiO_2 micromotors (44–66 μm s^{-1}, Video S3, Supporting Information) was higher than that of Fe_2O_3@MnO_2@SiO_2 motors (22–27 μm s^{-1}, Video S4, Supporting Information). This was attributed to the more violent O_2 generation by MnO_2 layers on the surface of FeO_x@MnO_2 nanoellipsoids (Figure S5, Supporting Information).

In addition, the relations between the motion speed and microstructures were further explored in 1 wt% H_2O_2 solution. As illustrated in Figure 5d and Video S5, Supporting

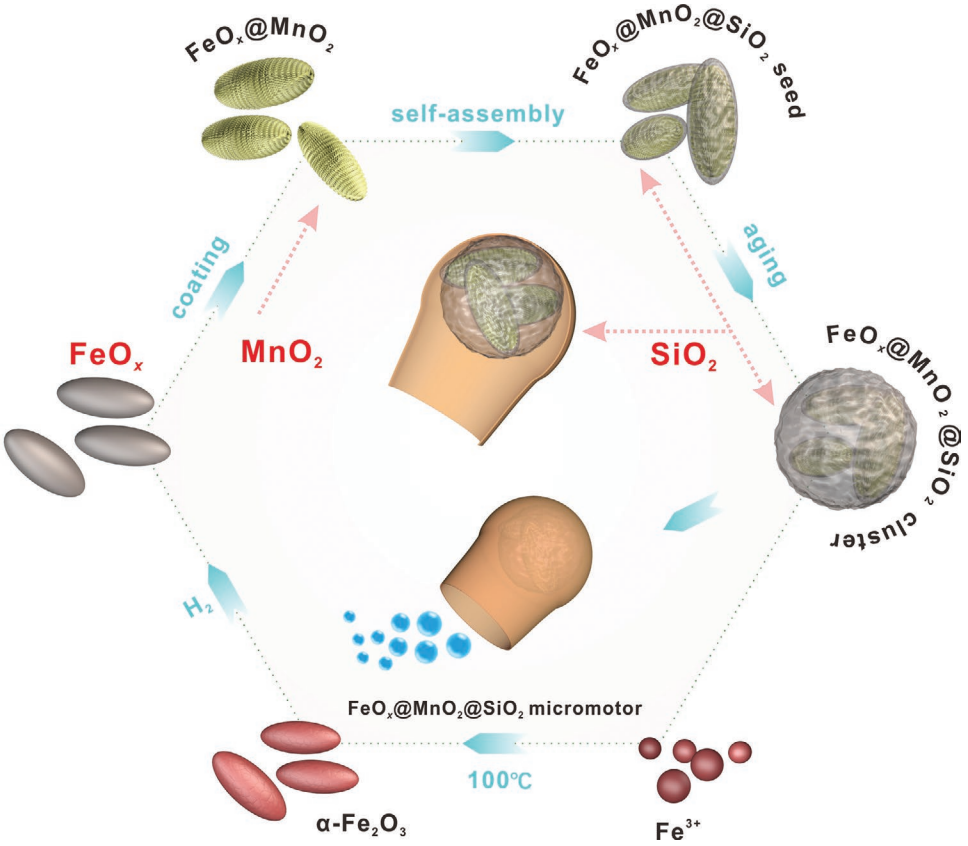

Figure 3. Proposed growth process of $FeO_x@MnO_2@SiO_2$ micromotors.

Information, the mean velocity of $FeO_x@MnO_2@SiO_2$-75 min motors (45 μm s^{-1}) was the highest among the micromotors with different aging periods, which was even much greater than $FeO_x@MnO_2@SiO_2$-60 min (35 μm s^{-1}) with the biggest opening (Figure 4b–f, Supporting Information). The slightly smaller opening of $FeO_x@MnO_2@SiO_2$-75 min is beneficial to providing a stronger propulsion force. The moving speeds decreased to 27 μm s^{-1} with 90 min aging and 11 μm s^{-1} at 120–180 min of aging, due to the long tails that prohibited sufficient solution exchange into the microenvironment of the cavity, as evidenced by the delayed movement of $FeO_x@MnO_2@SiO_2$-150 min in Video S5, Supporting Information.

Furthermore, the influence of solution pH_0 on the motion speed in the presence or absence of PMS was also considered. At pH_0 4.0 without PMS, the velocity (5.0–21.0 μm s^{-1}) halved compared to the uncontrolled tests but with a similar variation in speed for the micromotors with different aging times (Video S6, Supporting Information, Figure 5e). Moreover, the speed increased from 0 μm s^{-1} (pH_0 = 3.5) to 63 μm s^{-1} (pH_0 = 5.0), and then dropped to 0 μm s^{-1} (pH_0 = 6.0) (Video S7, Supporting Information), which may be attributed to the pH variation during the Fenton-like reaction of $FeO_x@MnO_2@SiO_2$-75 min/H_2O_2 system. After adding PMS, the velocity declined dramatically, due to the complexation of PMS with active Mn sites (forming $Mn^{(II,\ III)}{}_{(s)}$–$(HO)OSO_3^-$ complexes) via inner-sphere interactions, thus mitigating H_2O_2 decomposition as shown in Figure S11, Supporting Information.[29]

2.3. Evaluation of Naproxen Degradation of $FeO_x@MnO_2@SiO_2$ Micromotors

Naproxen, an antibiotic, is a widely known drug to treat non-selective, non-steroidal anti-inflammation.[30] However, naproxen usage in over 40 years has induced pharmaceutical-associated wastewater pollution, which poses a threat to the ecosystem due to its hydrophilicity and resistance to microorganisms.[30,31] Antibiotics could be removed from wastewater via adsorption or degradation by light irradiation or peroxides.[31–33] In conventional Fenton/Fenton-like reactions, H_2O_2 will be activated to generate free radicals (e.g., •OH and $O_2^{\bullet-}$) to oxidize the organic pollutants.[34] PMS can be activated into •OH, $SO_4^{\bullet-}$ or nonradical catalyst–PMS complexes.[35] Therefore, H_2O_2 decomposition (to O_2) and Fenton/Fenton-like processes (to generate ROS) will compete for the peroxides. In this work, we aim to establish the correlations between motion velocity and oxidation capacity of micromotors. With the highest moving capability, $FeO_x@MnO_2@SiO_2$-75 min was used to examine the catalytic performance of naproxen degradation in the PMS/H_2O_2 system without mechanical stirring. The micromotors did not swim in the solution below pH_0 4 and above pH_0 5.5 (Figure 5e). Thus, we compared the naproxen oxidation at pH_0 4.0–5.5. In Figure S12a, Supporting Information, the self-propelled micromotor attained the highest naproxen oxidation at pH_0 4.0, thanks to its lower final solution pH (3.8) compared to final pH above 7 for pH_0 4.5–5.5 (Figure S12b, Supporting

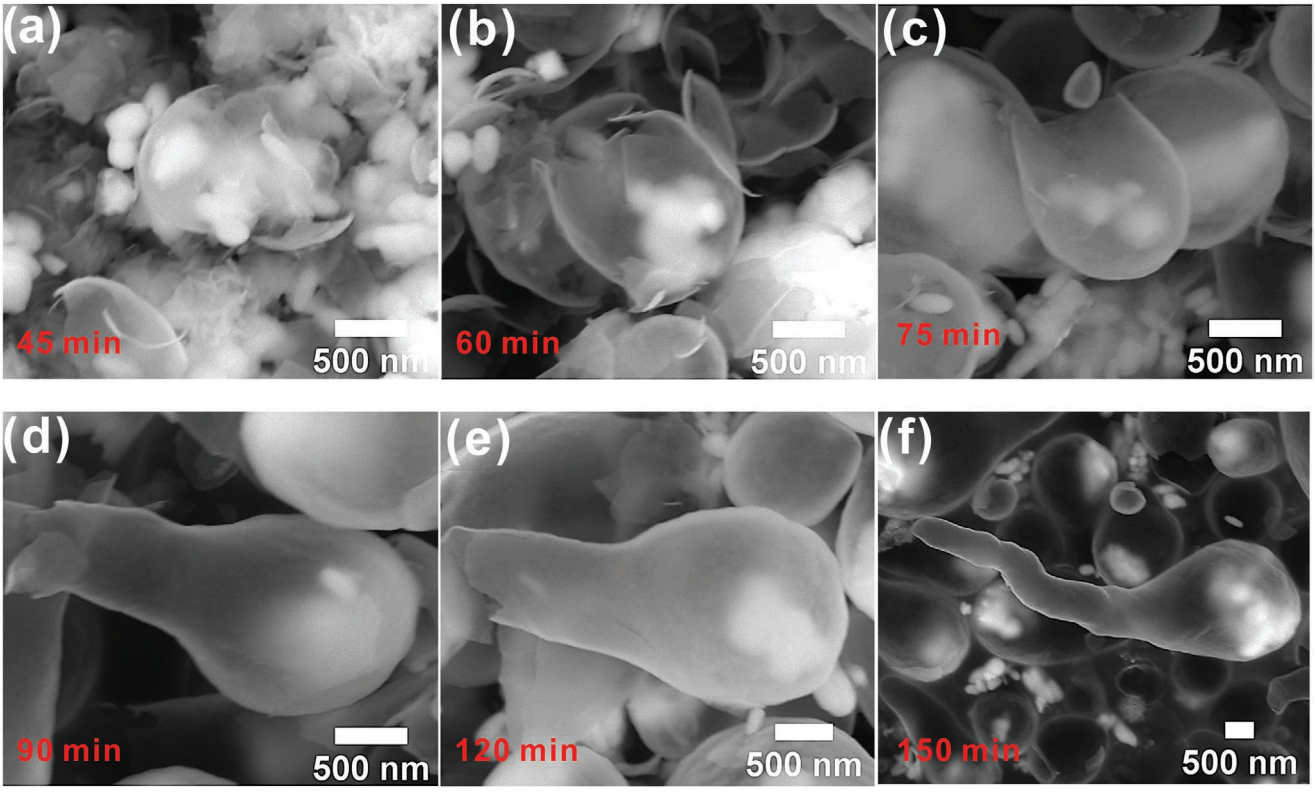

Figure 4. SEM images of FeO_x@MnO_2@SiO_2 micromotors at different aging time: a) 45, b) 60, c) 75, d) 90, e) 120, and f) 150 min.

Information). The acidic environment is favorable for Fenton-like reactions to generate more ROS.[36] Thus, pH_0 4.0 was used to evaluate naproxen degradation in the following experiments.

Both FeO_x@MnO_2@SiO_2 micromotors (**Figure 6**a) and H_2O_2 (Figure S13, Supporting Information) could not oxidize naproxen, and sole PMS removed 14% of naproxen in 60 min due to its stronger oxidation potential (1.82 V) (Figure S13, Supporting Information).[37] With the co-existence of H_2O_2 and PMS, the oxidation efficiency of naproxen changed marginally (13%), suggesting that H_2O_2 did not react with or dramatically affect the oxidation capacity of PMS (Figure S13, Supporting Information). Only 14% of naproxen was removed after 60 min but with a higher reaction rate in the first 30 min in the micromotor/PMS systems, indicating that micromotors without the fuel (H_2O_2) for agitation cannot effectively oxidize naproxen (Figure 6a). Additionally, 7% of naproxen was oxidized by micromotors/H_2O_2, indicating that the system can generate a small number of ROS via Fenton-like reactions. The oxidation efficiency phenomenally increased in the FeO_x@MnO_2@SiO_2/PMS/H_2O_2 system (77%), which was much higher than Fe_2O_3@MnO_2@SiO_2/PMS/H_2O_2 (40%).

To investigate the different catalytic activity for the two micromotors, we analyzed the degradation performances of different seeds (e.g., Fe_2O_3, Fe_2O_3@MnO_2, FeO_x, and FeO_x@MnO_2) in Figure S14, Supporting Information. Specifically, FeO_x removed more naproxen (50%) than Fe_2O_3 (37%) due to the presence of rich Fe(II) species that are active in H_2O_2/PMS-based Fenton-like reactions.[38] This explains the better degradation performance of the FeO_x@MnO_2@SiO_2 micromotor. However, after coating MnO_2 layers, both Fe_2O_3@MnO_2 and FeO_x@MnO_2 oxidized less naproxen in the PMS/H_2O_2 system (17% and 21%, respectively). The declined degradation efficiency was due to the faster H_2O_2 decomposition into O_2 by MnO_2, thus decreasing ROS generation due to insufficient peroxides (Figure S15c,e, Supporting Information). Moreover, the generation of violent bubbles on MnO_2 surface would inhibit the direct interaction between Fe_2O_3/FeO_x with peroxides. With the protection of outer SiO_2 microcapsules, FeO_x@MnO_2@SiO_2 micromotors consumed less H_2O_2 and generated more ROS for naproxen removal (Figure S15a, Supporting Information). In addition, these catalysts decomposed more H_2O_2 in the absence of PMS (Figure S15b,d, f, Supporting Information), leading to more powerful motion (Figure 5f). Thus, the mobility of micromotors was closely related to the catalytic performance of naproxen degradation.

Figure S16a,b, Supporting Information, demonstrates the naproxen removal by FeO_x@MnO_2@SiO_2 micromotors with different aging durations in the PMS/H_2O_2 system. The order of oxidation efficiency is FeO_x@MnO_2@SiO_2 was –75 min > –60 min ≈ –90 min > –120 min ≈ –180 min > –150 min. Notably, the micromotors experienced two-stage kinetics of naproxen degradation (Figure S16b, Supporting Information). The reaction rate at 5–15 min ($k1$) was much higher than that at 20–60 min ($k2$). The kinetics was affected by the pH variation (Figure S17, Supporting Information). Briefly, after adding FeO_x@MnO_2@SiO_2 micromotors, the solution pH sharply increased from 4.0 to 7.8 within 10 s in the presence of PMS and H_2O_2, and then declined to 4.0 at 20 min, finally reaching

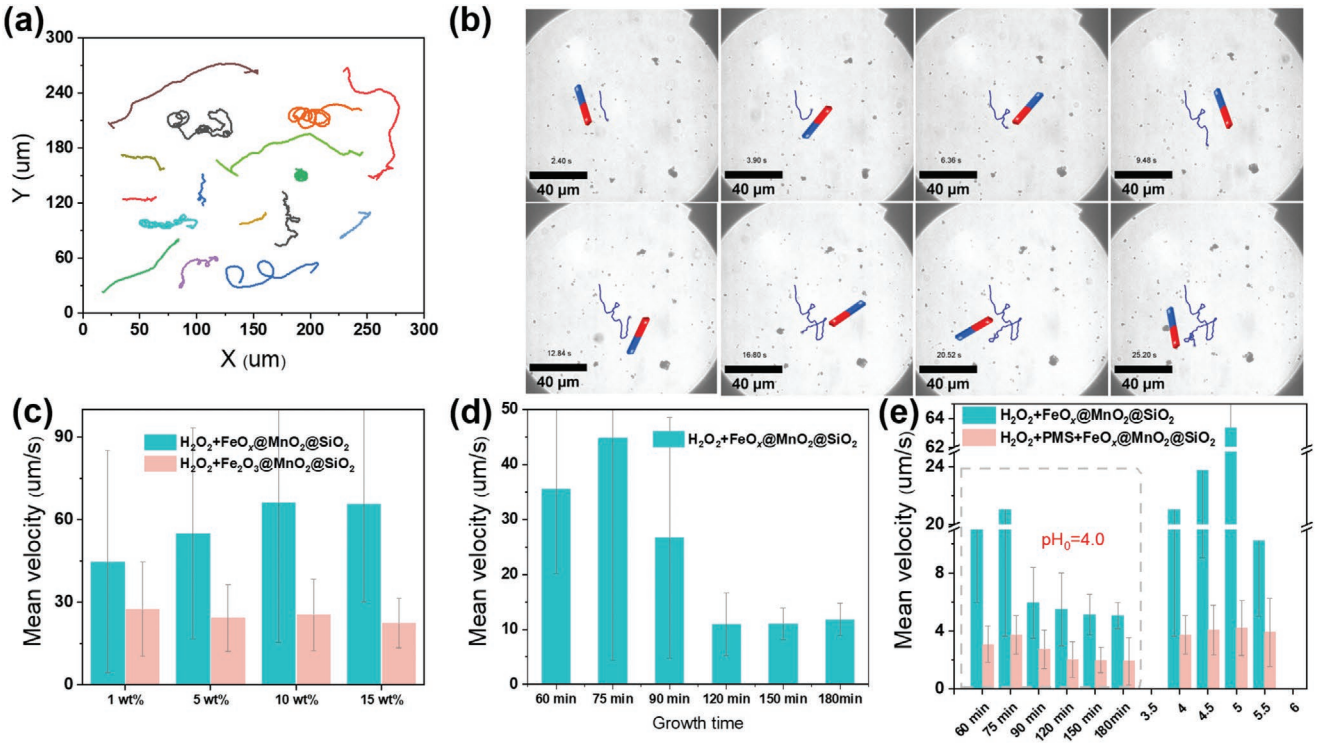

Figure 5. a) Motion trajectories of FeO_x@MnO_2@SiO_2 micromotors at 1 wt% of H_2O_2 solution; b) time-lapse images of FeO_x@MnO_2@SiO_2 micromotors guided by a magnet in 1 wt% of H_2O_2 solution; c) mean velocity of Fe_2O_3@MnO_2@SiO_2 and FeO_x@MnO_2@SiO_2 micromotors at different H_2O_2 concentrations without controlling the solution pH_0; d) mean velocity of FeO_x@MnO_2@SiO_2 micromotors with different aging time at 1 wt% of H_2O_2 without controlling the solution pH_0; e) mean velocity of FeO_x@MnO_2@SiO_2 micromotors with different aging time in H_2O_2 (1 wt%) or H_2O_2/PMS (1 wt%/1 mM) solution with controlling the solution pH_0 4.0, and different pH_0 (the aging time of the material was 75 min).

3.8 at 60 min. Thus, the higher speed at the stage of above pH_0 4.0 would promote antibiotic removal (Figure 5e). However, in the solo H_2O_2 system, the solution pH increased to 7.7 after adding micromotors and remained a relatively steady platform (7.8–8.0). The mechanisms of the variations in pH and kinetics are discussed as follows[39]

$$\equiv Fe^{2+} + H_2O_2 \rightarrow \equiv Fe^{3+} + {}^{\cdot}OH + OH^- \quad (2)$$

$$\equiv Fe^{3+} + H_2O_2 \rightarrow \equiv Fe^{2+} + O_2^{\cdot-} + 2H^+ \quad (3)$$

According to Equation (2), Fenton-like H_2O_2 decomposition will generate massive OH^- species, which will elevate the solution pH. Due to continuous H_2O_2 activation in the absence of PMS (Figure S15a,b, Supporting Information), the minor contribution of Equation (3) cannot consume the excessive hydroxide ions, thus reaching a high equilibrium pH 7.8; the process only exerted a 7% of naproxen removal in micromotors/H_2O_2 (Figure 6a). However, more hydrogen ions would be generated via Equation (3) due to the sluggish H_2O_2 decomposition by PMS in micromotors/H_2O_2/PMS.

In addition, the pH variation of FeO_x@MnO_2 nanoellipsoids in different systems (H_2O_2, PMS, or H_2O_2/PMS) was detected (Figure S18, Supporting Information). The solution pH also increased to 8.2 within 5 min, with the rapid and complete consumption of H_2O_2 (Figure S15d, Supporting Information), and the pH decreased to 7.1 in the system of FeO_x@MnO_2/H_2O_2. Without the protection of SiO_2 microcapsules, FeO_x@MnO_2 nanoellipsoids directly reacted with H_2O_2 and generated massive O_2 bubbles on the MnO_2 surface, affecting the liquid-solid reactions between FeO_x and H_2O_2 in the FeO_x@MnO_2/H_2O_2/PMS system. In this process, Equation (3) was inhibited, resulting in the continuous increase of pH from 5.8 (15 min) to 7.0 (60 min) with only 21% naproxen removal (Figure S14, Supporting Information). In contrast, solution pH in PMS/FeO_x@MnO_2 (Figure S18, Supporting Information) and PMS/FeO_x@MnO_2@SiO_2 (Figure S17, Supporting Information) experienced negligible change, resulting from the negligible change of the acidic PMS, which stabilized the solution pH (Figure S19, Supporting Information).

To investigate the relation between the motions of micromotors and the oxidation efficiency of naproxen, we carried out the fitting analysis between mean velocity and reaction rate (Figure 6b). The reaction rate (k) increased with the rise of mean velocity. It is indicated that naproxen oxidation was increased due to the enhanced solution mass transfer at a relatively low speed. In addition, the gradual slowdown of self-motion during the degradation reaction (Video S8, Supporting Information) was due to the declined solution pH from 7.8 to 3.8, according to Equation (3) (Figure S17, Supporting Information), led to a higher $k1$ value than $k2$. The larger slope of the fitting line of $k1$ further indicated that more violent movement was beneficial for naproxen removal. In the batch experiment, the micromotor was swimming during the antibiotic degradation in the H_2O_2/PMS solution for both FeO_x@MnO_2@SiO_2 (Video S8, Supporting Information) and FeO_x@MnO_2 (Video S9, Supporting

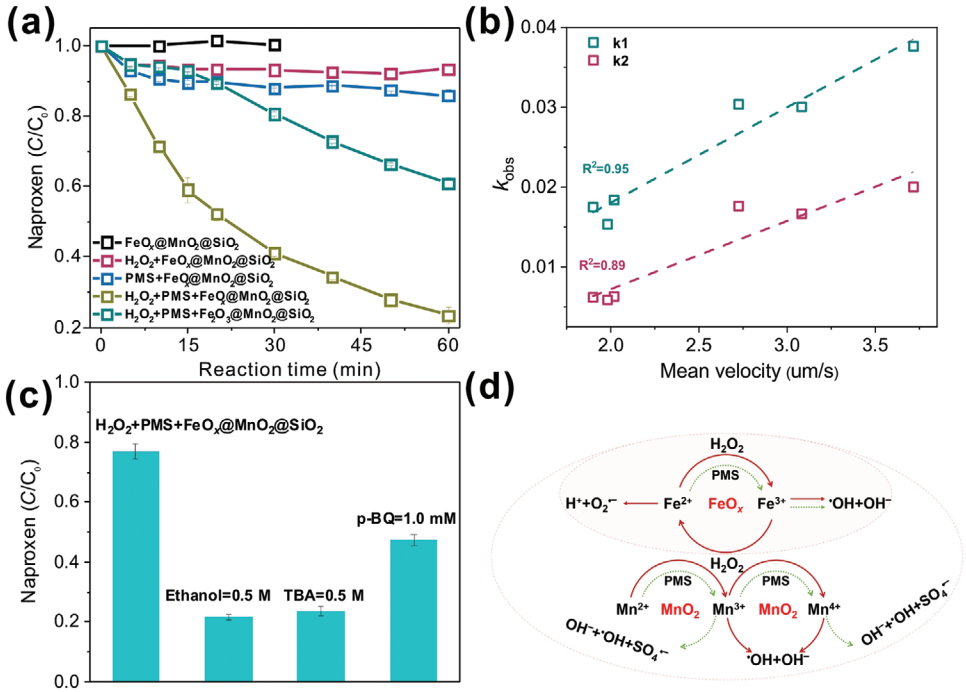

Figure 6. a) Catalytic degradation performance of naproxen by micromotors; b) the correlation between first-order reaction rate constant and velocity upon the micromotors with different aging time in the H_2O_2/PMS system; c) effect of various quenchers on naproxen oxidation; d) scheme of radical generation in the H_2O_2/PMS system by FeO_x and MnO_2. Experimental conditions: $[Naproxen]_0$ = 5 ppm, $[micromotors]_0$ = 0.5 g L^{-1}, $[PMS]_0$ = 1 mM, $[H_2O_2]_0$ = 1 wt%, pH_0 = 4.0, $[ethanol]_0$ = $[TBA]_0$ = 500 mM, $[p\text{-}BQ]_0$ = 1.0 mM, and reaction time = 60 min.

Information). Although more H_2O_2 was decomposed, FeO_x@MnO_2@SiO_2 micromotor kept moving after 60 min in the presence of solo H_2O_2 (Video S10, Supporting Information). As shown in Videos S8–S10, Supporting Information, more giant bubbles formed at the bottom of the containers and then raised to the liquid level, which was also monitored by optical microscopy (Video S11, Supporting Information). This phenomenon was caused by the partially aggregated micromotors. These reactive aggregates would sink toward the bottom first due to the gravity and subsequently generate bigger bubbles to separate the micromotors and induce solution micromixing (Figure S20, Supporting Information). In the microreactor, SiO_2 microcapsules provided a confined environment for the oxidation reaction, and the FeO_x@MnO_2 seeds produced ROS and O_2 bubbles to promote the mass transfer of peroxides and pollutant between the microreactor and macroenvironment (surrounding solution). The self-motion and bubble-induced micromixing would accelerate faster solution exchange, achieving rapid antibiotic degradation in the micromotors/PMS/H_2O_2 system.

Further, to verify the catalytic mechanism of naproxen oxidation, we carried out quenching experiments in the micromotors/PMS/H_2O_2 system in Figure 6c (derived from Figure S21, Supporting Information). Ethanol, tert-butanol (TBA), and p-benzoquinone (p-BQ) as quenchers can respectively identify the contributions of ($SO_4^{\bullet-}$ and $^{\bullet}OH$), $^{\bullet}OH$, and $O_2^{\bullet-}$ species.[40] About 77% of naproxen was oxidized by FeO_x@MnO_2@SiO_2 micromotors with the absence of quenchers. With additions of ethanol, TBA, and p-BQ, naproxen removals were at 21%, 24%, and 47%, respectively, implying that free radicals (e.g., $SO_4^{\bullet-}$, $^{\bullet}OH$, and $O_2^{\bullet-}$) dominated naproxen degradation in the micromotors/PMS/H_2O_2 system. Electron paramagnetic resonance (EPR) tests also confirmed the formation of $^{\bullet}OH$ and $O_2^{\bullet-}$ (Figure S22, Supporting Information). However, the signals of DMPO-SO_4 were not detected due to the insignificant yield of $SO_4^{\bullet-}$. In the system of micromotors/H_2O_2, signals of DMPO-OH were found and the signals of DMPO-O_2^- were not detected; seven typical peaks referred to 5, 5-dimethylpyrrolidone-2-(oxy)-(1) (DMPOX, the oxidation product of DMPO) were observed.[41] Without H_2O_2, no radical peaks were detected for micromotors/PMS. We further perform the quenching experiments to confirm the ROS in different systems.

We used FeO_x@MnO_2 seeds, the active components, to investigate the potential ROS in the solo- or dual-peroxide(s) systems. As shown in Figure S23a, Supporting Information, the oxidation efficiency of naproxen in the FeO_x@MnO_2/PMS system (no motion, 29%) was slightly higher than that in the FeO_x@MnO_2/PMS/H_2O_2 system (self-motion, 21%). In addition, only 6% of naproxen was removed in the presence of FeO_x@MnO_2 and H_2O_2, further indicating that violent bubble generation on the catalyst surfaces prohibited the interaction with antibiotics and the subsequent degradation. With the additions of ethanol and TBA, the catalytic performances of naproxen oxidation declined in PMS/H_2O_2 and PMS systems, suggesting that PMS were decomposed to produce $SO_4^{\bullet-}$ or ($SO_4^{\bullet-}$ and $^{\bullet}OH$) (Figure S23b,c, Supporting Information) via Equations (4) and (5).[42]

$$\equiv M^n + HSO_5^- \rightarrow \equiv M^{n+1} + SO_4^{\bullet-} + OH^- \quad (4)$$

$$SO_4^{\bullet-} + OH^- \rightarrow SO_4^{2-} + {}^{\bullet}OH \quad (5)$$

where M referred to metal oxides. In Figure S23d, Supporting Information, the naproxen removal decreased after adding ethanol (4%) and p-BQ (3%). The result suggests the contributions of $^{\bullet}OH$ and $O_2^{\bullet-}$ from H_2O_2 via Fenton/Fenton-like reactions. Notably, due to the PMS activation by p-BQ,[43] more naproxen (40%) was degraded in the PMS/H_2O_2 system (Figure S24b, Supporting Information).

Generally, both MnO_2 and FeO_x were able to trigger the generation of $SO_4^{\bullet-}$, $^{\bullet}OH$, and $O_2^{\bullet-}$ in the presence of PMS or H_2O_2.[6,44] Thus, the solo component in micromotors were investigated in different systems with the presence of different quenchers (Figures S24 and S25, Supporting Information). For MnO_2, similar naproxen removal efficiency (10%) was attained for PMS/H_2O_2 and PMS, which was higher than that of H_2O_2 (6%) (Figure S24a, Supporting Information). With the additions of ethanol and TBA, MnO_2 exerted 4% and 7% of naproxen removal, respectively (Figure S24b, Supporting Information), indicating the generation of $SO_4^{\bullet-}$ and $^{\bullet}OH$ in the co-presence of PMS and H_2O_2. In the MnO_2/PMS system, TBA (7% of naproxen oxidation) quenched more free radicals than ethanol (9%), indicating that a less amount of $SO_4^{\bullet-}$ and $^{\bullet}OH$ species were generated without the self-motion (Figure S24c, Supporting Information). In Figure S24d, Supporting Information, the addition of TBA decreased the efficiency of naproxen degradation in the MnO_2/H_2O_2 system. Yet, the oxidation efficiency experienced a marginal variation after adding p-BQ, which suggested that MnO_2 would produce $^{\bullet}OH$ radicals according to Equation (2) without forming $O_2^{\bullet-}$ species in the MnO_2/H_2O_2 system.

In regarding to FeO_x without self-motion in all systems, the catalytic efficiency of naproxen removal (H_2O_2/PMS) slightly increased in the first 40 min (H_2O_2) due to the contribution of PMS (Figure S25a, Supporting Information). In addition, the lower naproxen degradation after adding ethanol in FeO_x/PMS/H_2O_2 and FeO_x/PMS systems indicated that minor or no $SO_4^{\bullet-}$ was generated and more $^{\bullet}OH$ was formed to attack naproxen (Figure S25b,c, Supporting Information). In the FeO_x/H_2O_2 system, TBA and p-BQ dramatically decreased naproxen oxidation, indicating the co-existence of $^{\bullet}OH$ and $O_2^{\bullet-}$ (Figure S25d, Supporting Information). Because p-BQ can activate PMS to generate $^1O_2$ and quench $^{\bullet}OH$ radicals rapidly (1×10^8 M^{-1} s^{-1} for $^{\bullet}OH$, 9.6×10^8 M^{-1} s^{-1} for $O_2^{\bullet-}$).[45] Thus, we use chloroform (5.4×10^7 M^{-1} s^{-1} for $^{\bullet}OH$, 3.0×10^{10} M^{-1} s^{-1} for $O_2^{\bullet-}$) as a more selective quencher of $O_2^{\bullet-}$.[45] As shown in Figure S26, Supporting Information, after adding 1.0 and 10 mM of chloroform, the naproxen oxidation experienced a slight variation in FeO_x@MnO_2@SiO_2/H_2O_2/PMS system, indicating the minor contribution of $O_2^{\bullet-}$ in Fenton-like reactions.

Figure 6d illustrates the proposed radical generation mechanisms in the presence of MnO_2 and FeO_x. The main ROS are $SO_4^{\bullet-}$, $^{\bullet}OH$, and $O_2^{\bullet-}$ radicals generated from both PMS and H_2O_2 triggered by MnO_2 (Equations (2), (4), and (5)) and FeO_x (Equations (2)–(5)) via Fenton-like reactions. Different from the dominant Fenton-like catalyst of FeO_x, the crucial role of MnO_2 is to decompose H_2O_2 to generate oxygen bubbles to propel the micromotors. Therefore, as shown in Figure S27, Supporting Information, FeO_x@MnO_2@SiO_2 is dual-functional in initiating microreactor self-motion and catalytic degradation of naproxen in the co-presence of PMS and H_2O_2. Regarding the functions of each component, 1) FeO_x was mainly responsible for ROS generation; 2) MnO_2 primarily decomposed H_2O_2 into O_2 bubbles, propelling micromotors in the solution; 3) the outer SiO_2 microcapsule provided an asymmetric vessel to trigger an unbalanced torque for self-motion; 4) the inner SiO_2 shells linked the seeds and attached them to the microcapsules. Besides, the SiO_2 shells of the seed clusters slightly blocked the interaction between MnO_2 and H_2O_2, which reduced the consumption of H_2O_2. In addition to generating radicals, PMS molecules partially occupy active Mn sites on the MnO_2 surfaces and form PMS–MnO_2 complexes via inner-sphere interaction. The complexes on Mn sites prohibited H_2O_2 decomposition, which slightly reduces the motion of the motors but suppresses the instant generation of large volumes of gas for sustained motion and ROS generation. Also, the regulated H_2O_2 decomposition preserves more H_2O_2 for Fenton-like reactions inside the microreactor. Thus, there is a trade-off between ROS generation and bubble generation considering the multiphase reactions. Introducing a small amount of PMS provides more ROS and regulates the oxygen generation speed (H_2O_2 decomposition rate), killing two birds with one stone. The well-designated shape further intensifies the torque of the micromotors for fast velocity and mass transfer with the surrounding environment.

To evaluate the realistic application in wastewater purification, we applied the micromotors for catalytic degradation of various water matrices with PMS and H_2O_2 (Figure S28, Supporting Information). Roughly 77% of naproxen was removed in the Milli-Q water at pH_0 4. The chlorine ions in the tap water are PMS activators[46] which caused a sharp increase in naproxen oxidation (98%) in 60 min. Moreover, the pH (6.0–6.3) of the tap water experienced marginal variation during the antibiotic degradation (Figure S29, Supporting Information). Thus, we used a boric buffer to maintain the solution pH 6.3, which resulted in similar reaction kinetics to the Milli-Q water, although boric buffer was reported to enhance PMS activation.[47] In addition, the FeO_x@MnO_2@SiO_2 micromotors can still work in river water, attaining 20% of naproxen removal in 60 min. The declined efficiency was impacted by various background substances (e.g., inorganic ions and organic matters) that substantially consume ROS or block the active sites.[29] Moreover, the magnetic micromotors could be collected by a magnet after the reaction (Figure S30, Supporting Information) for reuse.

3. Conclusions

We synthesized bubble-propelled and magnetically steerable FeO_x@MnO_2@SiO_2 micromotors via a multi-step strategy for effective self-motion and antibiotic oxidation in the PMS/H_2O_2 system. The inner lamellar MnO_2 surfaces coated on the magnetic FeO_x (α-Fe_2O_3/Fe_3O_4) nanoellipsoids were responsible for decomposing H_2O_2 to form O_2 to propel micromotors in the solution. The outer SiO_2 microcapsule with an opening covered the FeO_x@MnO_2 seeds and built an asymmetric Janus structure to steer the torque. The addition of PMS inhibited the violent bubble generation on the MnO_2 surfaces via partially occupying the Mn active sites and thus promoted the contact

between solution (PMS/H_2O_2) and inner FeO_x to generate more ROS via Fenton-like reactions. Thereby, shape-controlled and multiple-component micromotors can achieve self-motion and efficient purification at the expense of low peroxide usage.

4. Experimental Section

Chemicals: All chemicals are of an analytical grade without further purification. OXONE ($KHSO_5{\cdot}0.5KHSO_4{\cdot}0.5K_2SO_4$, a source of PMS), ferric chloride hexahydrate ($FeCl_3{\cdot}6H_2O$), potassium permanganate ($KMnO_4$), sodium dihydrogen phosphate (NaH_2PO_4), polyvinylpyrrolidone (PVP, average molecular weight 40 000), ethanol, sodium citrate, ammonium hydroxide solution ($NH_3{\cdot}H_2O$, 28.0–30.0% NH_3 basis), tetraethylorthosilicate (TEOS), sodium hydroxide (NaOH), sulfuric acid (H_2SO_4), sodium sulfate (Na_2SO_4), sodium bicarbonate ($NaHCO_3$), potassium iodide (KI), tert-butanol (TBA), p-benzoquinone (p-BQ), and 5,5-dimethyl-1-pyrroline N-oxide (DMPO) were purchased from Sigma-Aldrich. Milli-Q water (18.2 MΩ·cm) was used in all the experiments.

Synthesis Procedures: α-Fe_2O_3 nanoellipsoids were synthesized via a modified method.[26] Specifically, 14 g $FeCl_3{\cdot}6H_2O$ and 100 mg NaH_2PO_4 were dissolved in 2 L water under ultrasonication for 20 min. Then, the solution was placed in an oven at 100 °C for 48 h, yielding dark red precipitates (α-Fe_2O_3) via hydrolysis of iron chloride. α-Fe_2O_3 was collected by several centrifugations and dried overnight at 60 °C. α-Fe_2O_3/Fe_3O_4 (FeO_x) nanoellipsoids were obtained via calcination at 400 °C for 1 h with a heating rate of 2 °C min^{-1} under a hydrogen atmosphere (5% of H_2/Ar). $FeO_x@MnO_2$ and α-$Fe_2O_3@MnO_2$ seeds were obtained via hydrothermal processes.[27] Typically, $KMnO_4$ solution (0.237 g, 30 mL) and α-Fe_2O_3 or FeO_x suspension solution (0.26 g, 30 mL) were mixed and transferred into a Teflon-lined autoclave (100 mL) at 160 °C for 24 h. After filtration and washing with ultrapure water, the sample was dried overnight at 60 °C. $FeO_x@MnO_2@SiO_2$ or α-$Fe_2O_3@MnO_2@SiO_2$ micromotors were synthesized via a mutual-template-assisted method.[17] In Figure S1, Supporting Information, 1 g polyvinylpyrrolidone (PVP) was dissolved in 30 mL of ethanol. First, sodium citrate solution and water were added to the PVP solution and stirred for 10 s (solution I). After adding $NH_3{\cdot}H_2O$, the mixture (solution II) was stirred for 10 s to obtain a stable emulsion system. Then seed solution was mixed for 30 s (solution III). Finally, tetraethylorthosilicate (TEOS) was added into solution III. After stirring for 10 s, the solution IV was obtained at different aging durations. In the synthesis of SiO_2 microcapsules, no seed was added. Cubic α-Fe_2O_3 was synthesized with the presence of the morphology indicator, Na_2SO_4.[26] Specifically, NaOH (6.0 M, 45 mL, 10.8 g) and $FeCl_3{\cdot}6H_2O$ (2.0 M, 50 mL, 27.03 g) were stirred for 5 min. Then Na_2SO_4 (10 mM, 5 mL, 7.1 mg) was added to the precursors with stirring for 10 min. The obtained solution was transferred into a Teflon-lined autoclave (inner volume: 200 mL) and maintained at 100 °C for 8 days.

Materials Characterizations: X-ray powder diffraction (XRD) was performed on a Bruker AXS D8 Advance X-ray diffractometer under Cu Kα radiation (λ = 1.54186 Å at 40 kV and 40 mA). The morphologies were characterized by an FEI Quanta 450 FEG environmental scanning electron microscope (SEM). The high-resolution transmission electron microscopy (HRTEM) images and scanning transmission electron microscopy (STEM) images with EDS mapping analysis were obtained from FEI Titan Themis incorporated in a JEOL 2100F microscope. Electron paramagnetic resonance (EPR) spectra were carried out using a Bruker EMX plus X-band CW ESR spectrometer.

Motion Characterizations: The solution was injected into a dish with a 12 mm diameter viewing area. The motion behavior was monitored by a Nikon Ti E live cell microscope. No surfactant was used in all experiments. Velocity tracking data were obtained from ten individuals to obtain the mean velocity by Image J software (Fiji).

Experimental Analysis: The solution samples were analyzed by ultrahigh performance liquid chromatography (UHPLC, Thermo Scientific) with a C-18 column and a UV detector. A 50 mL testing system was conducted in a 100 mL beaker with naproxen (5 ppm), catalyst (0.5 g L^{-1}), H_2O_2 (1 wt%), and PMS (1.0 mM) at 23 °C. During set time intervals, 1 mL solution was withdrawn through a 0.22 µm polyether sulfone filter, and then quickly injected into an HPLC vial with 20 µL ethanol. Rate constants (k_{obs}) were calculated based on the pseudo-first-order kinetic model.

$$\ln\left(\frac{C}{C_0}\right) = -k_{obs}t \tag{6}$$

Where, C_0 is the initial concentration of the organic, C is the concentration of the organic at time t and k_{obs} is the first-order reaction rate constant. The model was evaluated by plotting $\ln(C/C_0)$ versus reaction time (t). The concentration of PMS in the solution was analyzed by an iodometric method (see Supporting Information).[29]

Supporting Information

Supporting Information is available from the Wiley Online Library or from the author.

Acknowledgements

The authors acknowledge the help from the analytical lab in the Faculty of Sciences, Engineering and Technology (SET) at The University of Adelaide. This work was supported by the Australian Research Council (DP190103548).

Open access publishing facilitated by The University of Adelaide, as part of the Wiley - The University of Adelaide agreement via the Council of Australian University Librarians.

Conflict of Interest

The authors declare no conflict of interest.

Data Availability Statement

The data that support the findings of this study are available from the corresponding author upon reasonable request.

Keywords

hydrogen peroxide, micromotors, organic degradation, peroxymonosulfate, self-motion

Received: December 12, 2022
Published online:

[1] L. Xu, F. Mou, H. Gong, M. Luo, J. Guan, *Chem. Soc. Rev.* **2017**, *46*, 6905.
[2] T. Hou, S. Yu, M. Zhou, M. Wu, J. Liu, X. Zheng, J. Li, J. Wang, X. Wang, *Nanoscale* **2020**, *12*, 5227.
[3] H. Ye, G. Ma, J. Kang, H. Sun, S. Wang, *Chem. Commun.* **2018**, *54*, 4653.
[4] H. Ye, J. Kang, G. Ma, H. Sun, S. Wang, *J. Colloid Interface Sci.* **2018**, *528*, 271.
[5] Y. Yang, K. Hu, P. Zhang, P. Zhou, X. Duan, H. Sun, S. Wang, *Small* **2021**, *17*, 2100927.

[6] J. Ma, S. Zhang, X. Duan, Y. Wang, D. Wu, J. Pang, X. Wang, S. Wang, *Chemosphere* **2021**, *267*, 129287.
[7] W. Liu, H. Ge, X. Chen, X. Lu, Z. Gu, J. Li, J. Wang, *ACS Appl. Mater. Interfaces* **2019**, *11*, 16164.
[8] R. Maria-Hormigos, M. Pacheco, B. Jurado-Sánchez, A. Escarpa, *Environ. Sci.: Nano* **2018**, *5*, 2993.
[9] H. Ye, S. Wang, Y. Wang, P. Guo, L. Wang, C. Zhao, S. Chen, Y. Chen, H. Sun, S. Wang, *Appl. Catal. B* **2022**, *314*, 121484.
[10] K. Villa, J. Parmar, D. Vilela, S. Sánchez, *ACS Appl. Mater. Interfaces* **2018**, *10*, 20478.
[11] K. Wang, E. Ma, H. Wang, *Adv. Mater. Interfaces* **2022**, *9*, 2200271.
[12] J. Yang, J. Li, X. Yan, Y. Lyu, N. Xing, P. Yang, P. Song, M. Zuo, *ACS Appl. Mater. Interfaces* **2022**, *14*, 6484.
[13] C. Chen, E. Karshalev, J. Guan, J. Wang, *Small* **2018**, *14*, 1704252.
[14] L. Soler, V. Magdanz, V. M. Fomin, S. Sanchez, O. G. Schmidt, *ACS Nano* **2013**, *7*, 9611.
[15] J. Parmar, K. Villa, D. Vilela, S. Sanchez, *Appl. Mater. Today* **2017**, *9*, 605.
[16] E. Ma, K. Wang, Z. Hu, H. Wang, *J. Colloid Interface Sci.* **2021**, *603*, 685.
[17] C. Li, J. Zhang, S. Wang, Z. Zhu, H. Li, A.-B. Xu, Y. Yu, X. Wang, J. Yao, L. Wang, *Chem. Mater.* **2019**, *32*, 575.
[18] M. Yan, L. Xie, J. Tang, K. Liang, Y. Mei, B. Kong, *Chem. Mater.* **2021**, *33*, 3022.
[19] B. Qiu, L. Xie, J. Zeng, T. Liu, M. Yan, S. Zhou, Q. Liang, J. Tang, K. Liang, B. Kong, *Adv. Funct. Mater.* **2021**, *31*, 2010694.
[20] C. Zhou, C. Gao, Z. Lin, D. Wang, Y. Li, Y. Yuan, B. Zhu, Q. He, *Langmuir* **2020**, *36*, 7039.
[21] T. Gao, J. Lin, L. Xu, J. Guan, *Nanomaterials* **2022**, *12*, 2049.
[22] T. Liu, L. Xie, J. Zeng, M. Yan, B. Qiu, X. Wang, S. Zhou, X. Zhang, H. Zeng, Q. Liang, *ACS Appl. Mater. Interfaces* **2022**, *14*, 15517.
[23] C. Chen, H. Wang, C. Han, J. Deng, J. Wang, M. Li, M. Tang, H. Jin, Y. Wang, *J. Am. Chem. Soc.* **2017**, *139*, 2657.
[24] Y. Ma, K. Lan, B. Xu, L. Xu, L. Duan, M. Liu, L. Chen, T. Zhao, J.-Y. Zhang, Z. Lv, *Nano Lett.* **2021**, *21*, 6071.
[25] M. Yan, L. Xie, B. Qiu, S. Zhou, T. Liu, J. Zeng, Q. Liang, J. Tang, K. Liang, D. Zhao, *ACS Nano* **2021**, *15*, 11451.
[26] T. Sugimoto, Y. Wang, H. Itoh, A. Muramatsu, *Colloids Surf. A Physicochem. Eng. Asp.* **1998**, *134*, 265.
[27] L. Zhu, Z. Chang, Y. Wang, B. Chen, Y. Zhu, W. Tang, Y. Wu, *J. Phys. Chem. A* **2015**, *3*, 22066.
[28] A. Kuijk, A. Van Blaaderen, A. Imhof, *J. Am. Chem. Soc.* **2011**, *133*, 2346.
[29] Y. Yang, P. Zhang, K. Hu, X. Duan, Y. Ren, H. Sun, S. Wang, *Appl. Catal. B* **2021**, *286*, 119903.
[30] D. Wojcieszyńska, U. Guzik, *Appl. Microbiol. Biotechnol.* **2020**, *104*, 1849.
[31] J. Wang, X. Duan, J. Gao, Y. Shen, X. Feng, Z. Yu, X. Tan, S. Liu, S. Wang, *Water Res.* **2020**, *185*, 116244.
[32] Y. Shang, X. Xu, B. Gao, S. Wang, X. Duan, *Chem. Soc. Rev.* **2021**, *50*, 5281.
[33] Y. Dong, C. Yi, S. Yang, J. Wang, P. Chen, X. Liu, W. Du, S. Wang, B.-F. Liu, *Nanoscale* **2019**, *11*, 4562.
[34] X. Duan, H. Sun, S. Wang, *Acc. Chem. Res.* **2018**, *51*, 678.
[35] X. Duan, H. Sun, Y. Wang, J. Kang, S. Wang, *ACS Catal.* **2015**, *5*, 553.
[36] P. Zhou, W. Ren, G. Nie, X. Li, X. Duan, Y. Zhang, S. Wang, *Angew. Chem., Int. Ed.* **2020**, *59*, 16517.
[37] F. Ghanbari, M. Moradi, *Chem. Eng. J.* **2017**, *310*, 41.
[38] Y. Zhu, R. Zhu, Y. Xi, J. Zhu, G. Zhu, H. He, *Appl. Catal. B* **2019**, *255*, 117739.
[39] J. He, X. Yang, B. Men, D. Wang, *J. Environ. Sci.* **2016**, *39*, 97.
[40] W. Ren, C. Cheng, P. Shao, X. Luo, H. Zhang, S. Wang, X. Duan, *Environ. Sci. Technol.* **2022**, *56*, 78.
[41] Y. Yang, P. Zhang, K. Hu, P. Zhou, Y. Wang, A. H. Asif, X. Duan, H. Sun, S. Wang, *Appl. Catal. B* **2022**, *315*, 121593.
[42] J. Wang, S. Wang, *Chem. Eng. J.* **2018**, *334*, 1502.
[43] Y. Zhou, J. Jiang, Y. Gao, J. Ma, S.-Y. Pang, J. Li, X.-T. Lu, L.-P. Yuan, *Environ. Sci. Technol.* **2015**, *49*, 12941.
[44] H. Zhou, J. Peng, J. Li, J. You, L. Lai, R. Liu, Z. Ao, G. Yao, B. Lai, *Water Res.* **2021**, *188*, 116529.
[45] J. Huang, H. Zhang, *Environ. Int.* **2019**, *133*, 105141.
[46] Y. Zhou, J. Jiang, Y. Gao, S.-Y. Pang, J. Ma, J. Duan, Q. Guo, J. Li, Y. Yang, *Water Res.* **2018**, *138*, 56.
[47] Z. Chen, Q. Wan, G. Wen, X. Luo, X. Xu, J. Wang, K. Li, T. Huang, J. Ma, *Sep. Purif. Technol.* **2021**, *256*, 117841.